

REPORT DOCUMENTATION PAGE				<i>Form Approved</i> OMB No. 0704-0188	
Public reporting burden for this collection of information is estimated to average 1 hour per response, including the time for reviewing instructions, searching existing data sources, gathering and maintaining the data needed, and completing and reviewing this collection of information. Send comments regarding this burden estimate or any other aspect of this collection of information, including suggestions for reducing this burden to Department of Defense, Washington Headquarters Services, Directorate for Information Operations and Reports (0704-0188), 1215 Jefferson Davis Highway, Suite 1204, Arlington, VA 22202-4302. Respondents should be aware that notwithstanding any other provision of law, no person shall be subject to any penalty for failing to comply with a collection of information if it does not display a currently valid OMB control number. PLEASE DO NOT RETURN YOUR FORM TO THE ABOVE ADDRESS.					
1. REPORT DATE (DD-MM-YYYY) 14-02-2017		2. REPORT TYPE Final Technical Report - CLIN 0001		3. DATES COVERED (From - To) 02/18/2016 - 02/14/2017	
4. TITLE AND SUBTITLE Dielectric Metamaterial Reflector				5a. CONTRACT NUMBER N00014-16-C-1023, CLIN 0001	
				5b. GRANT NUMBER	
				5c. PROGRAM ELEMENT NUMBER	
6. AUTHOR(S) Srini Krishnamurthy				5d. PROJECT NUMBER	
				5e. TASK NUMBER	
				5f. WORK UNIT NUMBER	
7. PERFORMING ORGANIZATION NAME(S) AND ADDRESS(ES) SRI International 333 Ravenswood Avenue Menlo Park, CA 94025				8. PERFORMING ORGANIZATION REPORT NUMBER	
9. SPONSORING / MONITORING AGENCY NAME(S) AND ADDRESS(ES) Office of Naval Research Attn: Dr. Peter Morrison, Code 352 875 North Randolph Street Arlington, VA 22203				10. SPONSOR/MONITOR'S ACRONYM(S)	
				11. SPONSOR/MONITOR'S REPORT NUMBER(S)	
12. DISTRIBUTION / AVAILABILITY STATEMENT Distribution A: Approved for Public Release; Distribution Unlimited					
13. SUPPLEMENTARY NOTES					
14. ABSTRACT The overall goal of this project is to develop paint-like and/or applique material with very high reflectivity and low absorptivity in near infrared region of electromagnetic spectrum. In this Year 1 of the project, we have designed metamaterial with an effective real-impedance of zero, which is predicted to have a reflectivity close to 100% at a chosen wavelength. We exploited Mie resonance in monodisperse wavelength-sized particles to achieve effectively zero real impedance. In our design, we choose the size of the non-absorbing dielectric spheres to achieve Mie resonance at the wavelength of interest, a dielectric coating thickness to maintain periodicity under self-assembly conditions, and transparent binder medium amenable to either paint-like material or applique. We have optimized the design by including nonlinear absorption, materials defects and thermal propagation for enhanced reflection and angular performance.					
15. SUBJECT TERMS all-dielectric, perfect reflection, metamaterial applique					
16. SECURITY CLASSIFICATION OF:			17. LIMITATION OF ABSTRACT SAR	18. NUMBER OF PAGES 33	19a. NAME OF RESPONSIBLE PERSON Srini Krishnamurthy
a. REPORT U	b. ABSTRACT U	c. THIS PAGE U			19b. TELEPHONE NUMBER (include area code) 650-859-4997

14 February 2017

Dielectric Metamaterial Reflector

Final Report for Period: 18 February 2016 – 14 February 2017
Contract # N00014-16-C-1023, CLIN #0001
SRI Project P23720

Prepared by:

Srini Krishnamurthy, PI
SRI International
Advanced Technology and Systems Division
650-859-4997
srini@sri.com

Prepared for:

Office of Naval Research
875 North Randolph Street
Arlington, VA 22203
Attn: Dr. Peter Morrison, Code 352

Distribution A: Approved for public release; distribution unlimited.

1. Overview of Project

The overall goal of this project is to develop paint-like and/or applique material with very high reflectivity and low absorptivity in near infrared region of electromagnetic spectrum.

Concept: The reflectivity at a given wavelength is 100% when the material has an effective real-impedance of zero. Mie resonance in monodisperse wavelength-sized particles can be used to introduce resonances in the effective permittivity (ϵ) and permeability (μ) to achieve either a negative real ϵ or a negative real μ . This ensures that the impedance, given by $(\mu/\epsilon)^{1/2}$, will have a near-vanishing real part, resulting in near-perfect reflection. In our design, we choose the size of the non-absorbing dielectric spheres to achieve Mie resonance at the wavelength of interest, a dielectric coating thickness to maintain periodicity under self-assembly conditions, and transparent binder medium amenable to either paint-like material or applique.

The specific objectives in the base year of the program are:

1. Optimize the reflector design for enhanced reflection and improved angular performance.
2. Calculate the nonlinear parameters such as two-photon absorption coefficient and free-carrier scattering cross section of the particle material.
3. Develop a comprehensive code to solve Maxwell's equations with nonlinear terms.
4. Evaluate the effect of material defects—voids and particle size—on the reflection property.
5. Solved coupled optical and thermal model for light propagation through absorptive medium.
6. Evaluate of the effect of nonlinear absorption on electric and magnetic resonances.

We achieved these objectives. The details are summarized below and detailed in Appendices A and B.

2. Completed Activities

Below we discuss in detail the activities we completed over the course of this project.

Designed metamaterial reflector: Single-negative metamaterials provide a promising approach for achieving high reflectivity. However, current designs require carefully designed features that can be obtained only by lithographic fabrication methods. We have designed a highly reflecting metamaterial that can be synthesized by self-assembly methods. By exploiting the Mie resonance in dielectric spheres and optimizing the sphere size and coating thickness, we applied full-wave simulations to obtain near-perfect reflection in the near-infrared spectral wavelength region. The details and the results of our systematic study on angular performance and the effect of coating thickness, particle size distribution, voids, and layer thickness on the reflectivity of the metasurface are described for possible publication and included here Appendix A.

Developed coupled optical and thermal model: We coupled the nonlinear optical model with a thermal solver to obtain the change in temperature as function of light absorption in the structured medium. This coupled model, limited to infinite periodic structures, is based on the microwave heating toolbox in COMSOL. The user guide for this model are described in Appendix B.

Investigated the impact of nonlinear absorption on Mie resonance: We applied our nonlinear full-wave model to study the fundamental impact of nonlinear absorption on Mie resonances in InP spheres. We found that nonlinear absorption dampens both the electric and magnetic resonance with the magnetic resonance (near 1.2 μm) showing greater damping owing to the larger free-carrier absorption cross

section associated with longer wavelengths. Since the intensity within the nanoparticle is enhanced at resonance, the metamaterial achieves the same nonlinear absorption as a homogeneous layer of the same thickness for an intensity 30 times lower. This effect could be exploited in several nonlinear absorption applications including optical limiting and frequency conversion. The results of this study have been summarized for possible publication and included here Appendix C.

Identified methods to synthesize InP & Si particles: Since the modeling study carried out thus far bodes well for meeting the reflection requirements, we completed a literature study for materials synthesis and layer deposition so that we are prepared to make progress immediately after optional funding is authorized. Our models indicate that InP particles with a diameter of 380 nm and a silica shell of thickness 60 nm will produce the desired coating response. This will be our baseline material. There are no commercial sources of such particles, so SRI will leverage methods in the literature to develop the desired materials in Years 2 and 3 of the proposed effort.

InP base particle: Two pathways to the synthesis of the InP base particle have been identified and will be investigated. One approach will seek to grow the InP crystals utilizing a synthetic strategy based on the controlled growth in solution under ambient pressure. The other approach will explore a recently reported solvothermal means to generate the base InP particle. It is likely that both of these approaches will utilize some form of annealing to achieve performance requirements regarding particle morphology and particle purity. SRI has unique fluidized bed capabilities that are well suited for this aspect of the project. The synthesis of InP nanocrystals with dimensions of <10 nm has been well studied and was the subject of a recent review [Chem. Mater., 2016, 28 (8), pp 2491–2506]. The interest in InP in this size range is due to their optoelectronic effects associated with quantum confinement. The review, while focused on nanocrystal development, provides significant input on the kinetics of particle growth and the effect that monomer concentration has on particle development. It also presents key insights that provide an understanding of factors involved in maintaining particle growth. Of major importance are control of precursor concentration, and once particle growth has been achieved it is important to quickly quench before the onset of Ostwald ripening, which will cause the particle size to defocus and broaden.

The main challenge for this aspect of the synthetic effort is developing a reactor design with a reactant feed system capable of maintaining precursor concentrations at a desired level. This will require some kind of input with respect to precursor concentration currently in the reactor. Preferably the precursor concentration will be determined in real time using an optical flow-through cell monitored by FTIR or UV-Vis spectroscopy. Alternatively, a rapid sample extraction and analysis protocol will be developed. The extraction and analysis approach allows for more analytical techniques to be considered, most notably gas chromatography to interrogate precursor concentrations and dynamic light scattering (DLS) to monitor particle size. This approach can also be automated to some extent with readily available sampling devices that will collect samples and subject them to analysis at predetermined intervals.

The solvothermal synthesis of InP particles in the range of 400 to 600 nm with a zinc blende structure has been reported in the literature [J. of Alloys and Compounds 472, 59 (2009); Materials Research Bulletin 44 (2009), 216–219]. This particle size is slightly larger than the size requirements based on modeling, and there is no information given regarding particle size distribution. However, there is sufficient information in the cited reference regarding the influence of reaction variables on the resultant particle phase and morphology to guide SRI's synthetic effort to generate the desired particle size and size distribution. Through an iterative process, SRI will develop a solvothermal protocol for the preparation of InP with the desired particle size and size distribution characteristics. Once a protocol is identified, work

will proceed to scale the process to multi-gram quantities. SRI has employed a similar approach in the development of rare-earth-doped ceramics particles for use in biodiagnostic applications. In the event the particle size distribution is large, SRI will employ a combination of sedimentation and/or field flow fractionation methods to narrow this distribution.

Silica coating: The next step in the particle synthesis is the application of a silica shell to the InP core particle. SRI has considerable experience using a modified Stöber process [J. of Colloid and Interface Science, 26, 62 (1968)] to apply a silica coating to a variety of different materials. This work has focused, for the most part, on the coating of upconverting phosphor particles in the 150–400 nm range [Analytical Biochem. 288, 176 (2001)]. In the case of the InP particles there are a number of literature precedents for the application of a silica coating [see for example, Silica-Coated InP/ZnS Nanocrystals as Converter Material in White LEDs, Advanced Materials, Volume 20, Issue 21, pages 4068–4073, November 3, 2008]. The fundamental difference in the reported silica coating protocol and those previously developed at SRI is that the InP requires the use of a surfactant to properly solvate, or “wet,” the surface of the nanoparticles such that uniform nucleation of the silica precursors is obtained, resulting in a uniform silica coating. The addition of a surfactant is a common technique used to facilitate the silica coating of nanoparticles with no, or very little, native oxide surface. The oxide surfaces are the nucleating sites typically exploited in the silica coating of nanoparticles. In this case, InP has very little native oxide and the surfactants actually bind to the surface and then serve as nucleating sites for the development of a uniform silica coating.

Ordered film formation: The ordered films will be generated using well-established evaporative techniques. The key features are the film growth compartment, in which the films are grown at the bottom by a combination of gravity and evaporation of a slurry containing the nanoparticles. The design incorporates a fluid thermal control compartment that will be utilized to control the temperature of the nanoparticle slurry and, along with headspace gas flow/control, will allow effective control of evaporation rates. The design also includes a glass window to enable monitoring of the film growth process. The cell design will allow films to be grown on substrates up to 2.5 cm x 2.5 cm. Once film generation parameters have been established at this length scale, efforts will focus on extending the substrate size. The parameters of importance are the density of the suspension solution and the evaporation rate of the suspension fluid. The density of the suspension fluid will control the sedimentation rates of the particles. Ideally the sedimentation rate will be such that particles will be able to sample many different configurations before finding the minimum associated with the formation of a quasi-crystalline material. If sedimentation is too fast, it is likely the defect rates will be high. Defect densities will be investigated using FESEM and TEM. In SRI's current understanding of the self-assembly process, the likelihood of being able to reduce any observed lattice defect structures in a post-assembly manner is low. Therefore, emphasis will be on fabricating the self-assembled structures in an optimal manner with an anticipated minimal time spent in attempting to anneal out any defects. Fortunately there is a significant interest in the utilization of self-assembly techniques in the generation of materials on a commercial scale that has received considerable attention in the literature. Recently several approaches have been put forth with respect to the generation of perfect colloidal crystal architectures (ACS Nano, 2016, 10, 5260–5271 and ACS Nano 2016, 10, 6791–6798). These approaches emphasize that optimal crystal formation is not achieved in a dynamic system and that a controlled stimulus can be utilized to both improve crystal quality and reduce growth time. Guidance from the theoretical analysis cited will be useful in developing the actual crystal growth protocols.

Film binder: It is anticipated that the films will be generated in an applique format, which will require some form of binder to hold the self-assembled structures together. The ability to wick in low viscosity materials into colloidal structures is known and commonly used to incorporate a binder material. Of key consideration in the binder selection is the optical absorption (must be 0 in the wavelengths of interest) and thermal properties (must have as high an operating temperature as possible). Assuming the absorption on the binder is negligible, the key factor in robustness of the coating will be the thermal stability of the binder system. Another consideration in a binder system would be the use of solventless formulations in which 100% of the infiltrated material is utilized. This avoids the issue of solvents and any residue they may leave behind. SRI recently contacted Dr. Keith Caruso at The John Hopkins Applied Physics Laboratory. Dr. Caruso has been investigating binder systems for high-temperature applications for ONR. His input on which binder systems to consider will be extremely valuable, and we will begin technical discussions with him soon.

Characterization: Characterization of the phase and elemental composition of the InP and silica-coated InP will be conducted by X-ray diffraction (XRD), energy dispersive X-ray spectroscopy (EDAX), and X-ray fluorescence (XRF). Particle size and size distribution analysis will be conducted by static (Horiba CAPA) and dynamic (Horiba LB220) light scattering as well as by field emission scanning electron microscopy (FESEM) and tunneling electron microscopy (TEM). Cross-sectional analysis by TEM of the silica-coated InP particles will provide details regarding the silica coating thickness and uniformity. Physical characterization of the metamaterial films will consist primarily of FESEM and TEM analysis to determine morphology of the particle arrays. We will use FESEM to examine film quality and will look at investigating the particle distribution in the film in both a front face and cross-sectional manner. Cross-sectional analysis will be assisted by embedding the film in an epoxy matrix and then polishing the cross-sectional areas to reveal the particle distribution in the film.

Silicon nanoparticles: Recent calculations indicate that Si particles could also be used in metamaterial synthesis. The possibility of utilizing Si particles in the construction of the coating was recently reconsidered in light of some experimental results from some micro-fabricated structures. The published information regarding the generation of Si particles is larger than that for InP due to the recent level of interest in Si nanoparticles in the Li battery industry. The synthetic strategies outlined in the literature utilize techniques SRI is well suited to investigate. Specifically, high-pressure solvothermal processing and the use of an RF-induced plasma coupled to a fluidized bed reactor have been utilized at SRI for 20+ years. As such, it would seem that Si particles may be easier to develop. However, when one considers the Si purity needed to prevent any absorption (estimated at >99.99%) the number of literature precedents decreases considerably. This is due to the fact that the Li battery application does not require such a high level of purity as the electronics industry or for the reflective application SRI has proposed. This does not preclude the use of some of the synthetic strategies utilized in the Li-battery application, but using these strategies will require special attention to the purity of input materials and any sources of impurities during processing.

Although we explored Si nanoparticles, we plan to continue our studies only with InP nanoparticles. Since InP continues to be an acceptable material for reflector application and our previously submitted options include the cost for only InP-based development, we will develop an InP-based metamaterial reflector.

3. Significance of Results

Our full-wave models indicate that the metamaterial designed in the program offer extremely high reflectivity with micron-thick metamaterial layer. The design and synthesis method enable applique-type approach for large area applications and specifically suited for Navy assets. In addition, our detailed calculations of the effect of nonidealities on optical and thermal properties provide confidence that nonidealities introduced during materials synthesis will not compromise performance, and bode well for a follow-on demonstration.

4. Publications

We have written two manuscripts for possible publication, subject to Navy's approval for public release. They are included as Appendixes A and C to this final report.

Appendix A

**Manuscript entitled “High Reflector Metasurface of Close-Packed Dielectric Spheres,”
prepared for possible publication in Applied Physics Letters**

Metamaterial Reflector of Close-Packed Dielectric Spheres

L. Zipp, B. Slovick, and S. Krishnamurthy

SRI International, Applied Optics Laboratory, Menlo Park, California 94025

Single-negative metamaterials provide a promising approach for achieving high reflectivity. However, current designs require carefully designed features that can be obtained only by lithographic fabrication methods. We present a design for a highly reflecting metamaterial that can be synthesized by self-assembly methods. By exploiting the Mie resonance in dielectric spheres and optimizing the sphere size and coating thickness, we apply full-wave simulations to obtain near-perfect reflection in the near-infrared spectral wavelength region. We report the results of our systematic study on angular performance and the effect of coating thickness, particle size distribution, voids, and layer thickness on the reflectivity of the metasurface.

There is a growing need for robust large-area high reflectivity coatings in applications including improved coatings in reflective telescopes and free space optical communication mirrors, optical sensor protection, and laser-powered spacecraft propulsion for missions such as the Breakthrough Starshot,¹ which aims to accelerate a micro-sized spacecraft to 20% of light speed using laser radiation pressure on a large reflective sail. Traditional metallic coatings cannot achieve the high reflectivity desired for such applications. Currently, high reflectivity (>99.9%) is achieved with dielectric multilayer coatings known as distributed Bragg reflectors (DBRs), and three-dimensional photonic crystals.² DBRs and photonic crystals achieve high reflection or photonic band gaps using Bragg scattering, or constructive interference of waves reflected by the periodic structure. The drawback of DBRs and photonic crystals is that they require expensive and delicate deposition and fabrication techniques, which preclude their application to large surface areas. Recently, subwavelength optical elements in the form of metasurfaces have been exploited for near-perfect reflection^{3,4,5} and other functions including metasurfaces have been designed for enhanced reflection and transmission,⁶ polarization splitting^{7,8} and control,⁹ focusing,¹⁰ beam steering,¹¹ and anomalous refraction.¹² However, these elements require lithographic fabrication methods, limiting their use to small, planar surfaces. Self-assembly based nanosphere lithography has been used to fabricate larger-scale metasurfaces,¹³ but the etching process limits this process to cm² areas.

There have been several studies and demonstrations of the optical properties of dilute as well as close-packed structures of dielectric spheres. Low-density colloidal suspensions of silicon spheres have been shown to exhibit highly efficient diffuse reflection.¹⁴ However, most applications require specular reflection. On the other hand, studies of dense, self-assembled, close-packed spheres have mostly focused on the photonic band structure arising from inter-particle

Bragg scattering arising from the periodicity.^{15,16,17,18} Interesting and complex behavior emerges when the spheres comprising the periodic structure also exhibit large single-particle Mie resonances, analogous to resonant scattering by a potential well in quantum mechanics. The single-particle resonances are modified by the presence of neighboring particles, and there is coupling between single-particle and diffractive resonances arising from the periodicity of the bulk structure.¹⁹ A two-dimensional hexagonal array of silicon spheres was shown to exhibit collective Mie-resonant behavior,¹⁴ but did not achieve near-unity reflectance because of the inability to tune and optimize the particle spacing.

In this Letter, we exploit Mie resonance in coated indium phosphide (InP) spherical particles to design a highly reflecting (>99.98%) hexagonally close-packed metamaterial layer. In contrast to previous designs, this metamaterial layer can be fabricated by self-assembly methods as a standalone appliqué layer for application on large-area and irregularly shaped surfaces. By harnessing single-particle Mie resonances and a thin oxide coating to control the particle separation, we are able to achieve greater than 99.98% reflectivity in the near-infrared (NIR) region with only three layers of hexagonal close-packed InP spheres. This is in contrast to traditional photonic crystals and multilayer stacks, which require many more layers to achieve such high reflectivity.

Since a large refractive index is required to obtain strong Mie resonances, we choose InP spheres (refractive index $n \approx 3.3$ for NIR wavelengths) in a polymer binding matrix ($n = 1.5$). The spheres are arranged in a hexagonal close-packed structure and the diameter, d , of the sphere is chosen to position the magnetic-dipole Mie resonance near the wavelength, λ_0 , for high reflection. For isolated spheres with large refractive index relative to the background medium, the magnetic-dipole Mie resonance occurs near $d = \lambda_0/n$, where n is the refractive index of the sphere,²⁰ but for

the close-packed structure the resonance is modified by the interaction between neighboring resonators. In addition, we consider a thin SiO_2 coating on the InP spheres, as shown in Fig. 1(a), to allow for tuning of the periodicity of the close-packed structure.

Using full-wave finite-element modeling (HFSS from Ansys), we optimized the diameter, coating thickness, and number of layers for high reflection at $1\ \mu\text{m}$. The calculated reflectance at normal incidence is shown in Fig. 1(b). For a single layer, the reflectance reaches close to 100%, but is narrowband. With additional layers, the high reflectance region broadens and shifts towards longer wavelengths. For 2 layers, the peak reflectivity is actually lower than for a single layer, due to the modification of the Mie resonance by the presence of neighboring spheres. For three layers the reflectance is already $> 99.9\%$ over a bandwidth of 50 nm, reaching over 99.98% reflectance in some regions. We find that the reflectivity continues to increase with additional layers, approaching near-unity reflection with increased bandwidth. Since the high reflectivity of the metasurface arises from single-particle Mie resonances, only a few layers of the spheres are required to achieve near-perfect reflection.

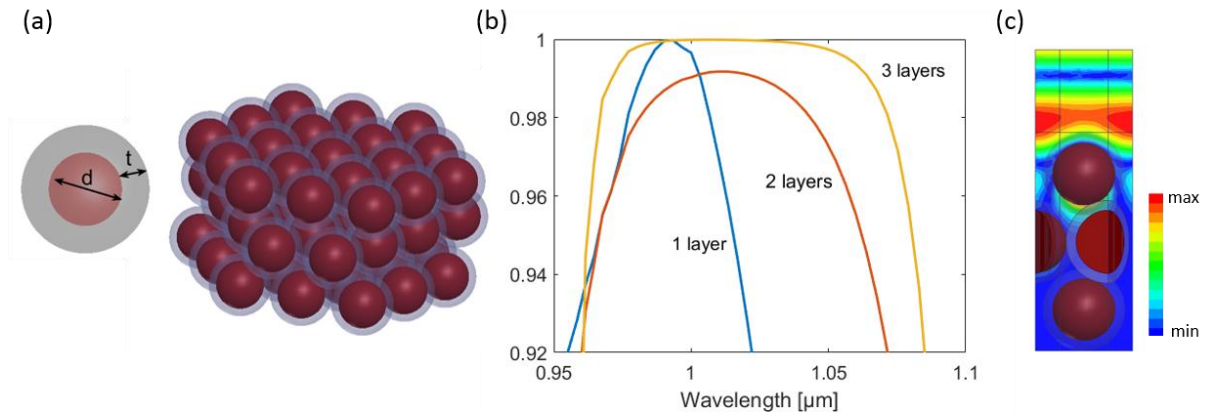


Figure 1. (a) Hexagonal close-packed high-index InP spheres with SiO_2 coatings. The structure consists of three layers of 360 nm indium-phosphide spheres with 60-nm-thick SiO_2 coatings on top of a transparent quartz substrate. (b) Normal incidence reflectance from the metasurface containing different numbers of layers. The reflectance is greater than 99.9% near $1\ \mu\text{m}$ for three layers over a bandwidth of 50 nm. (c) Spatial distribution

To further understand the optical properties of the metasurface, we plot in Fig. 1(c) the spatial distribution of the electric field magnitude in the three layer metasurface. The electric field does not penetrate beyond the first layer of spheres, confirming that the use of single-particle resonances negates the need for many layers as in DBRs. In addition, the electric field attains a maximum at the surface of the top layer of spheres, unlike in conventional reflectors. This behavior is expected for a magnetic mirror²¹, since the electric field does not undergo a π phase shift upon reflection, as in conventional electrical conductors. The maximum electric field at the reflecting surface can be exploited in applications such as low profile antennas, imaging bio tissues, and surface-enhanced Raman spectroscopy (SERS).^{22,23,24}

A key feature of the reflector design is the ability to optimize the periodicity of the hexagonal close-packed structure by tuning the thickness of the silicon dioxide coating on the InP spheres. When the oxide thickness is reduced, the close packing requirement reduces the periodicity as well and the reflectance spectrum is considerably changed, as illustrated in Fig. 2(a) for a single layer design. For a relatively large shell thickness of 200 nm, the electric and magnetic dipole Mie resonances of the spheres occur near 1.1 μm and 1.2 μm respectively. This is confirmed by plotting the electric field vectors at these two resonant wavelengths, as shown in Fig. 2(c-d). At 1.1 μm , the electric field is enhanced within the InP sphere and exhibits the characteristics of a typical dipole field, while at 1.2 μm , the electric field displays a large circulating component, consistent with the presence of a magnetic dipole. As the shell thickness is reduced and the periodicity decreases, the electric and magnetic Mie resonances are shifted towards shorter wavelengths, and the magnetic dipole resonance broadens significantly. This behavior is due to the interaction of the Mie resonance between neighboring spheres. For a shell thickness of 60 nm, the magnetic dipole resonance is sufficiently widened for use as a broadband high reflector metasurface. The tunability

of the reflectance spectrum with the oxide shell thickness is also possible for multiple layers as shown in Fig. 2(b) in which the reflectivity for three layers of the spheres on a quartz substrate for different coating thicknesses is plotted. Decreasing the thickness of the coating results in a blueshift of the high reflectance region, due to the decrease in lattice periodicity. The importance of the silicon dioxide coating in the design can be seen by comparing the reflectance of the metasurface with no coating ($t=0$ nm, dotted blue curve), to designs with finite coating thickness. In the absence of a coating, the reflectance properties of the metasurface suffer considerably due to leakage of the normal component of electric field into adjacent spheres, which dampens the Mie

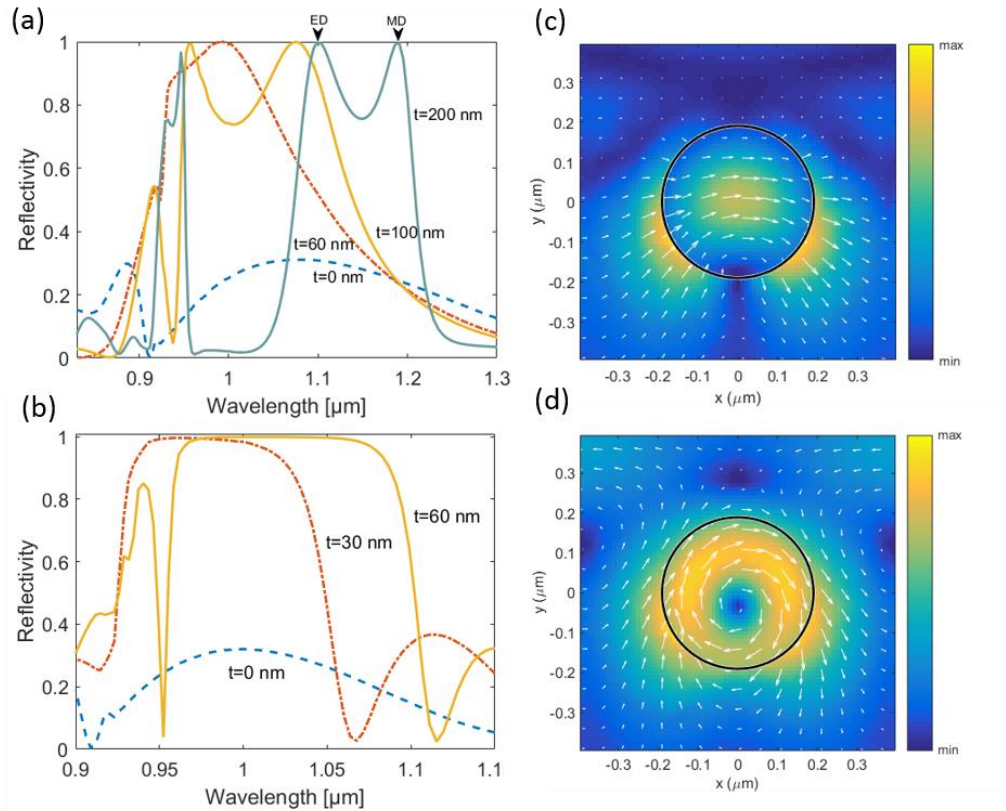


Figure 2. (a) Reflectance for a single layer of hexagonal close-packed spheres for different shell thicknesses t . The electric dipole and magnetic dipole Mie resonances for a 200-nm coating are denoted “ED” and “MD,” respectively. (b) Reflectance for different thicknesses with three layers of close-packed spheres at normal incidence on a quartz substrate. Panels (c) and (d) show the electric field vectors of the electric (c) and magnetic (d) dipole Mie resonances for a 200-nm-thick coating. The black circle denotes the boundary of the 360-nm-diameter InP sphere.

resonance. The presence of even a 30-nm-thick shell eliminates the coupling and near-perfect reflectance is achieved.

We now study the angle-dependent reflection performance, shown in Fig. 3(a). For dielectric spheres with a 60 nm coating, high reflectivity at 1 μm is maintained up to 10° before dropping steeply. For TE polarized light (electric field vector perpendicular to the plane of incidence), the reflectance remains remarkably high ($>99.9\%$) for all angles of incidence, while reflectivity suffers for TM polarized light (electric field vector in the plane of incidence). The TM mode reflectance displays a sharp cutoff and drops rapidly to zero, in contrast to normal homogenous materials which show a gradual variation in the reflectivity as a function of angle. The cause of this sharp cutoff can be understood by comparing the reflectance spectrum of the TM mode at various angles of incidence, shown in Fig. 3b. As the angle of incidence increases, the high reflectance band region shifts towards longer wavelengths, causing the TM polarized reflectance to drop to zero at lower wavelengths. Consequently, the average reflection decreases to very low values beyond a

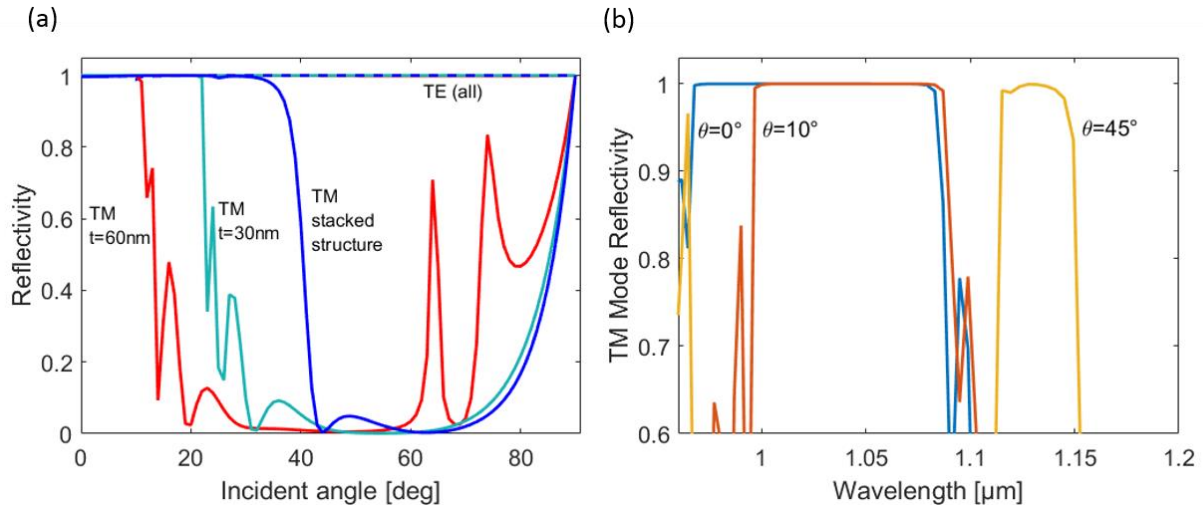


Figure 3. (a) Reflectance versus angle of incidence on a 7-layer structure of spheres on a quartz substrate, with two different silicon dioxide shell thicknesses, as well as a combined “stacked” structure containing two differently designed metalayers. The stacked structure consists of three layers of spheres with $d=360$ nm and $t=30$ nm and four layers of spheres with $d=330$ nm and $t=45$ nm. (b) Reflectance spectrum of the TM polarization mode for $d=360$ nm $t=60$ nm at different angles of incidence showing a redshift at steeper angles of incidence.

certain angle. Multilayer films also exhibit a redshift with increasing angle of incidence, suggesting that this behavior derives from the resonant elements or layers. We further note from Fig. 3a that the angular performance at a chosen wavelength can be increased with appropriate choice of coating thickness. We can reduce the shell thickness to move the center wavelength of reflection to lower values and use higher angle to move that to higher wavelength, allowing to high reflection at the center wavelengths for larger angles. This is seen for a 30-nm shell coating, where we find that the high reflectivity region can be extended out to 20 degrees. To extend the angular coverage beyond 20 degrees, we can use a stacked layer approach. For example, we modeled a seven-layer structure in which the top three layers contain 360-nm-diameter InP spheres coated with 30-nm-thick SiO₂ in a polymer binder, while the bottom four layers are composed of 330-nm-diameter spheres with a 45-nm-thick SiO₂ coat. We find (Fig. 3(a)) that with this structure, high reflectance can be extended past 30 degrees. With additional layers, the angular performance can be further improved.

We envision that the layers will be made by a self-assembly process followed by polymer backfill and peel-off from the substrate for applying to surfaces of interest. Since both the self-assembly process and the particle synthesis invariably lead to voids and size distribution, we study the impact of these defects on reflectance. We consider one vacancy in a supercell of 12 atoms per layer (equivalently 8.3% defect density). The calculated reflectivity in the NIR band from one layer with defects is reduced considerably (Fig. 4(a), dashed line). However, the reflectivity is nearly fully recovered at the designed wavelengths when one defect-free layer is added above the defective layer (Fig. 4(a), solid line). If the void is in the top layer on the other hand, even the normally incident light is scattered into the perfect layer below at various angles, resulting in lower reflectivity. High reflection can be regained only by adding several more defect-free layers. This

result can be qualitatively understood as the incident light scattering off the vacancy defect²⁵ into the lower layers of the metasurface. When the defect in the top layer cannot be avoided, the backfilled composite can be peeled off, inverted, and applied to the surface of interest. This ensures that the top layer as applied to the surface is completely filled, providing maximum reflectivity.

The supercell-based calculations are not ideally suited for studying the impact of particle size distribution, as the size of the supercell required is too large to be computationally efficient. We have evaluated only the limited effect of size variation by calculating the reflectivity with one smaller-sized sphere in a 12-sphere supercell on the top layer. The bottom layers are defect-free. This situation would occur for lower size defect densities of the order of a few percent, representing the tails ($>2\sigma$) of a Gaussian size distribution curve. The predicted reflectivity as a function of the defective sphere size is plotted in Fig. 4(b). The reflectance decreases by less than 1% for a 30-nm reduction in diameter, corresponding to a one-sided tolerance of 8% in sphere size variation. This level of tolerance is within the achievable bounds of current nanosphere production techniques.¹⁴

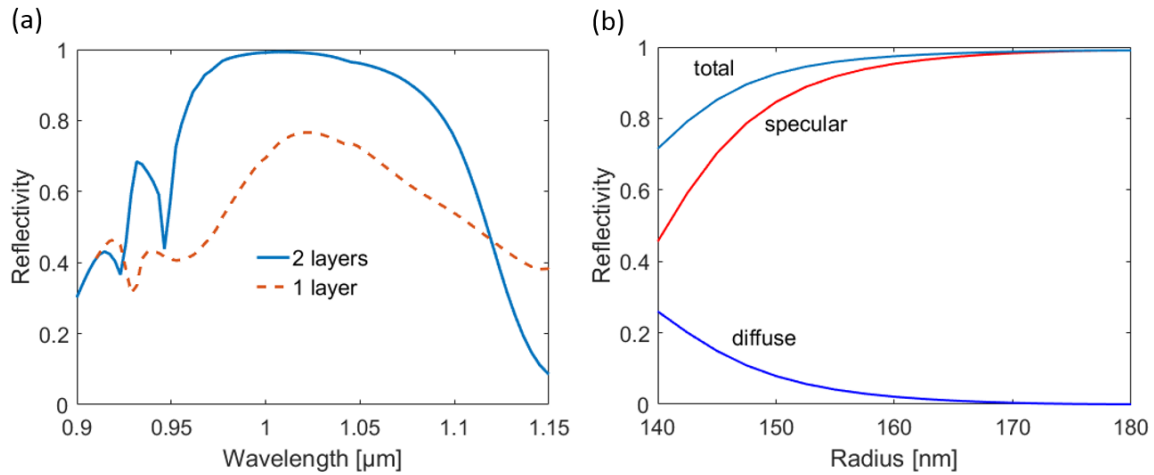


Figure 4. (a) Calculated reflectance for a single layer of spheres with 8.3% vacancy defects compared to that with a perfect layer above. (b) Reflectance as a function of size of one defect particle in 12-particle unit cell on the top layer. The bottom layer is assumed defect free.

In summary, the self-assembled dielectric sphere metasurface studied here represents a robust, scalable, high-reflectivity coating that can be applied to large and irregularly shaped surfaces. The design offers distinct advantages over multilayer coatings and other metasurface approaches. We have shown that the design parameter space is large enough to increase reflectance and angular performance and mitigate the effect of defects. The simplicity of the construction and its robust properties suggests that it may provide a cost-effective solution for high-reflectivity, low-absorption coatings.

The authors gratefully acknowledge funding for this research from the Office of Naval Research through Contract N00014-16-C-1023.

References:

- 1 <https://breakthroughinitiatives.org/Initiative/3>
- 2 E. Yablonovitch, T.J. Gmitter, and K.M. Leung, *Phys. Rev. Lett.* 67, 2295 (1991).
- 3 F. Namin, S. Yun, T.S. Mayer, D.H. Werner, and C. Rivero-Baleine, in 2011 IEEE Int. Symp. Antennas Propag. APSURSI (2011), pp. 1155–1158.
- 4 B. Slovick, Z.G. Yu, M. Berding, and S. Krishnamurthy, *Phys. Rev. B* 88, 165116 (2013).
- 5 P. Moitra, B.A. Slovick, Z.G. Yu, S. Krishnamurthy, and J. Valentine, *Appl. Phys. Lett.* 104, 171102 (2014).
- 6 P. Spinelli, M.A. Verschuuren, and A. Polman, *Nat. Commun.* 3, 692 (2012).
- 7 W. Guo, G. Wang, T. Li, H. Li, Y. Zhuang, and H. Hou, *J. Phys. Appl. Phys.* 49, 425305 (2016).
- 8 B.A. Slovick, Y. Zhou, Z.G. Yu, I.I. Kravchenckou, D.P. Briggs, P. Moitra, S. Krishnamurthy, and J. Valentine, *ArXiv161004040 Phys.* (2016).
- 9 H.F. Ma, G.Z. Wang, G.S. Kong, and T.J. Cui, *Sci. Rep.* 5, 9605 (2015).
- 10 M. Khorasaninejad, W.T. Chen, R.C. Devlin, J. Oh, A.Y. Zhu, and F. Capasso, *Science* 352, 1190 (2016).
- 11 S. Sun, K.-Y. Yang, C.-M. Wang, T.-K. Juan, W.T. Chen, C.Y. Liao, Q. He, S. Xiao, W.-T. Kung, G.-Y. Guo, L. Zhou, and D.P. Tsai, *Nano Lett.* 12, 6223 (2012).
- 12 C. Pfeiffer and A. Grbic, *Phys. Rev. Lett.* 110, 197401 (2013).
- 13 P. Moitra, B.A. Slovick, W. li, I.I. Kravchencko, D.P. Briggs, S. Krishnamurthy, and J. Valentine, *ACS Photonics* 2, 692 (2015).
- 14 L. Shi, J.T. Harris, R. Fenollosa, I. Rodriguez, X. Lu, B.A. Korgel, and F. Meseguer, *Nat. Comm.* 4, 1904 (2013).
- 15 F. Meseguer, *Colloids Surf. Physicochem. Eng. Asp.* 270–271, 1 (2005).
- 16 A. Blanco, E. Chomski, S. Grabtchak, M. Ibisate, S. John, S.W. Leonard, C. Lopez, F. Meseguer, H. Miguez, J.P. Mondia, G.A. Ozin, O. Toader, and H.M. van Driel, *Nature* 405, 437 (2000).
- 17 Y. Xia, B. Gates, Y. Yin, and Y. Lu, *Adv. Mater.* 12, 693 (2000).
- 18 G.I.N. Waterhouse and M.R. Waterland, *Polyhedron* 26, 356 (2007).
- 19 A.B. Evlyukhin, C. Reinhardt, A. Seidel, B.S. Luk'yanchuk, and B.N. Chichkov, *Phys. Rev. B* 82, 045404 (2010).

- 20 M.S. Wheeler, J.S. Aitchison, and M. Mojahedi, *Phys. Rev. B* 73, 045105 (2006).
- 21 S. Liu, M.B. Sinclair, T.S. Mahony, Y.C. Jun, S. Campione, J. Ginn, D.A. Bender, J.R. Wendt, J.F. Ihlefeld, P.G. Clem, J.B. Wright, and I. Brener, *Optica* 1, 250 (2014).
- 22 M. Esfandyarpour, E.C. Garnett, Y. Cui, M.D. McGehee, and M.L. Brongersma, *Nat. Nanotechnol.* 9, 542 (2014).
- 23 S.B. Choi, D.J. Park, S.J. Byun, J. Kyoung, and S.W. Hwang, *Adv. Opt. Mater.* 3, 1719 (2015).
- 24 Z. Ma, S.M. Hanham, P. Albella, B. Ng, H.T. Lu, Y. Gong, S.A. Maier, and M. Hong, *ACS Photonics* 3, 1010 (2016).
- 25 A.F. Koenderink, A. Lagendijk, and W.L. Vos, *Phys. Rev. B* 72, 153102 (2005).

Appendix B

COMSOL User Guide to Study High-Intensity Light Propagation Through Structured Media

COMSOL User Guide to Study High-Intensity Light Propagation Through Structured Media

First, open a new file by selecting Model Wizard, select 3D, and select Electromagnetic Waves, Frequency Domain (emw). Click Add and then Study, and then under Preset Studies, select Frequency Domain and click Done. This loads the COMSOL user interface, shown in Fig. 1, which consists of four setup sections shown on the left-hand side of the window: Global Definitions, Components, Study, and Results. Global Definitions is where the frequency-dependent material properties are defined, such as the permittivity of InP, as well as parameters defining the geometry such as radius and shell thickness. The Components section consists of defining the geometry of the structure, assigning materials to the geometry, applying boundary conditions and excitations, and meshing the design. The Study section is where frequency and parameter sweeps are defined, and Results is where plots are generated.

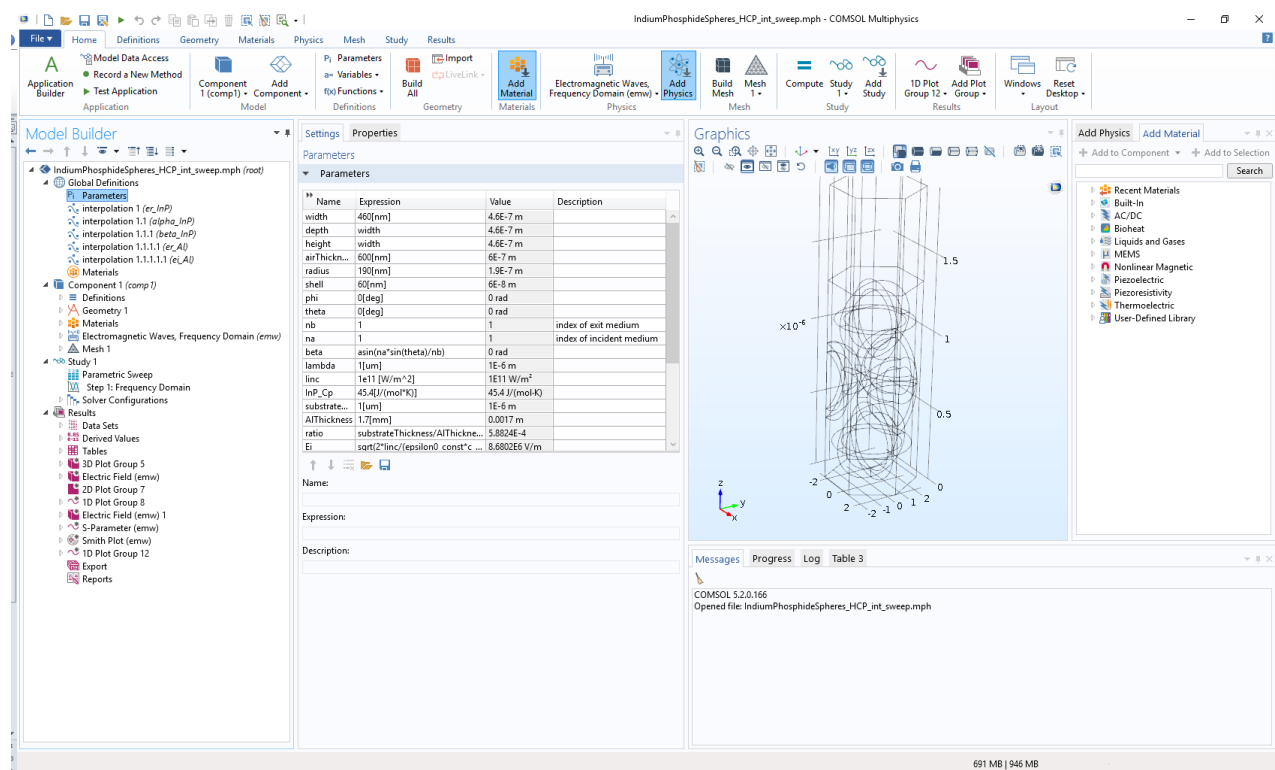


Figure 1. COMSOL user interface.

Starting with the Global Definitions, the first step is to define the frequency-dependent optical properties of InP and the Al substrate. Start by creating either a text or csv file with one column giving the frequency in Hz and the second column giving the optical property. Next, right-click Global Definitions and select Functions and then Interpolation. Near the middle of the window is a folder icon called Load from File. Select this and load the file with the optical properties. Also specify the function name under Definition. Repeat this process for all frequency-dependent properties, including permittivity and absorption coefficient.

Next, the geometry must be defined within the Component section. For the hexagonal close-packed array of spheres, the unit cell is a hexagon. Start by right-clicking Geometry and selecting Work Plane. Draw

the hexagon within the work plane and then use the Extrude feature to form a volumetric hexagon, as shown in Fig. 1. Next, draw the spheres by right-clicking Geometry and selecting Spheres. Choose their coordinates within the unit cell to form the close-packed geometry. Next, the region of the spheres outside the hexagonal volume must be removed. This is done using the intersection operation within Boolean and Partitions by right-clicking Geometry. Within the settings of the intersection, select the sphere and hexagonal volume and click Build All Objects to remove the portion of the sphere outside the volume.

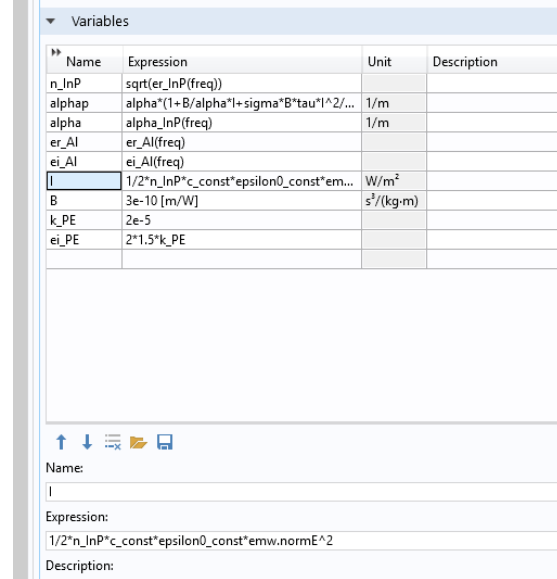
The next step is to define a few local variables within the component section, as shown in Fig. 2. Here we can define, for example, the refractive index n_{InP} as the square root of the frequency-dependent permittivity of InP, which we defined earlier in Global Definitions. The most important step for the nonlinear solver is to define the intensity-dependent absorption coefficient of InP, called α_{ph} . The effective intensity-dependent permittivity of InP can be written as

$$\varepsilon(I) = n^2 - j \frac{n}{k_0} \alpha'(I), \quad (4)$$

where n is the refractive index and $\alpha'(I)$ is an effective absorption coefficient given by $\alpha' = \sigma N_0 [1 + \beta I / (\sigma N_0) + \sigma \beta \tau I^2 / (2 \hbar \omega \sigma N_0)]$ and the various parameters are defined in the report. The intensity is related to the local electric field by $I = 1/2 n c \varepsilon_0 |\mathbf{E}|^2$. As shown in Fig. 2, we defined the intensity in terms of the absolute value of the electric field emw.normE . Then the absorption coefficient α_{ph} was defined in terms of this intensity variable.

The next step is to assign material properties to the geometry. This step is straightforward. For example, define a material by right-clicking Materials. Within the settings of the new material, define the permittivity, which for InP will be of the form of Eq. (x) above. Note that the permittivity property accepts complex quantities so the absorption can be included here. Once the properties are defined, select the appropriate domains within the geometric entity selection window.

Next up are the boundary conditions and excitations within the Components section. T- assign periodic boundary conditions, right-click Electromagnetic Waves, Frequency Domain and select Periodic Condition. Within the settings of the periodic condition, select opposite faces of the unit cell, as shown in Fig. 3. Repeat this for the other four faces of the hexagonal unit cell.



Name	Expression	Unit	Description
n_{InP}	$\sqrt{\text{er_InP}(\text{freq})}$		
α_{ph}	$\alpha_{\text{ph}}(1 + B/\alpha_{\text{ph}} I + \sigma \beta \tau I^2 / (2 \hbar \omega \sigma N_0))$	1/m	
α_{ph}	$\alpha_{\text{ph}}(\text{freq})$	1/m	
er_Al	$\text{er_Al}(\text{freq})$		
ei_Al	$\text{ei_Al}(\text{freq})$		
I	$1/2 * n_{\text{InP}} * c_{\text{const}} * \epsilon_{0_{\text{const}}} * \text{emw.normE}^2$	W/m ²	
B	$3e-10 \text{ [m/W]}$	s ² /(kg-m)	
k_{PE}	$2e-5$		
ei_PE	$2 * 1.5 * k_{\text{PE}}$		

Figure 2. Variables within the component section, showing how the nonlinear effects are included by defining the intensity in terms of the electric field variable emw.normE and then defining an intensity-dependent absorption coefficient.

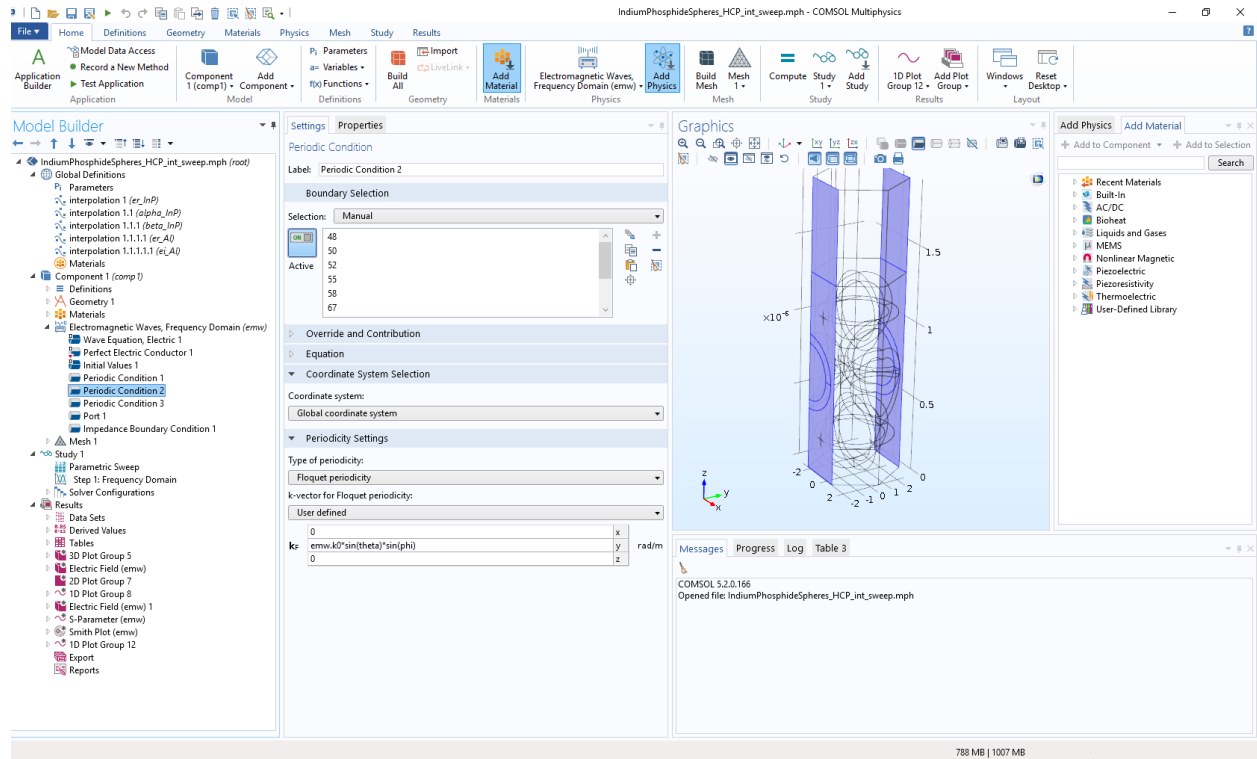


Figure 3. Assignment of periodic boundary conditions.

To set up the plane wave excitation, right-click Electromagnetic Waves, Frequency Domain and select Port. Within the port settings in Boundary Selection, select the top face of the unit cell where the light will be entering. To specify the incident power, within the Boundary Selection window, shown in Fig. 4, uncheck Specify Deposited Power and type the expression shown in Fig. 4, which is the product of the incident intensity, defined as a global variable, and the area of the hexagonal unit cell. Next, define the incident polarization using the x, y, and z values within the electric mode field. Lastly, define the propagation constant as shown in terms of the solution variable $emw.k0$. This is the propagation constant at the source.

Our simulations assume an Al substrate that can be modeled using an impedance boundary condition. This can be assigned to the bottom face by right-clicking Electromagnetic Waves, Frequency Domain. The optical properties can be assigned by calling the frequency-dependent permittivity values into the Relative Permittivity field within the Impedance Boundary Condition properties. Specifically, we defined variables within the Component section called er_Al and ei_Al , corresponding to the real and imaginary parts of the Al permittivity, which are equal to the

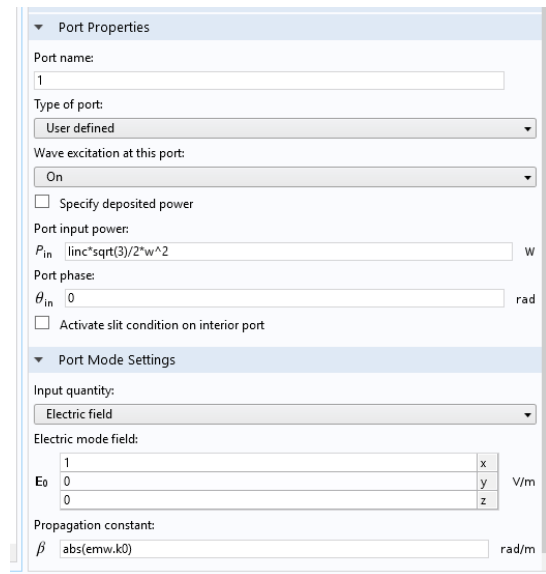


Figure 4. Port excitation properties, including input power and polarization.

frequency-dependent functions defined in the Global Definitions. The permittivity is then typed into the impedance boundary condition as $\epsilon_{r_Al-1j} \cdot \epsilon_{i_Al}$.

The next step is to define the mesh properties. First, right-click Mesh and select Size. Within the Element Size window of Size, select normal for the predefined mesh. Next, right-click mesh, go to More Operations, and select Free Triangular. Within the Boundary Selection of Free Triangular, select all of the faces on one side of the unit cell, as shown in Fig. 5.

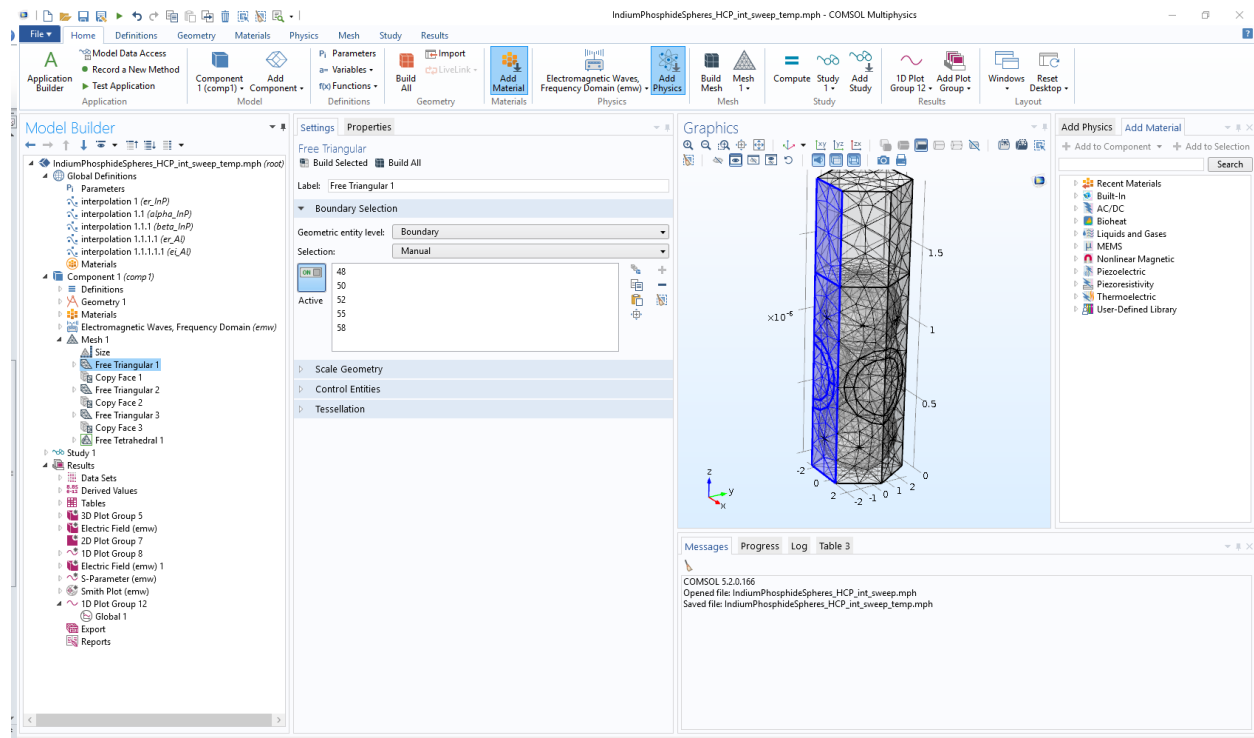


Figure 5. Assigning a mesh to one face of the unit cell.

Next, right-click Mesh, go to More Operations, and select Copy Face. Within Copy Face properties, for the source Boundaries select the same faces used in the Free triangular field shown in Fig. 5. Then in the Destination Boundaries, select the faces on the opposite side of the unit cell, as shown in Fig. 6. This copies the mesh generated on the face shown in Fig. 5 to the opposite face. Repeat this process for the other two face pairs. Lastly, right-click Mesh and select Free Tetrahedral. Within the Domain Selection of Free Tetrahedral, select Remaining. Click Build Mesh to render the mesh.

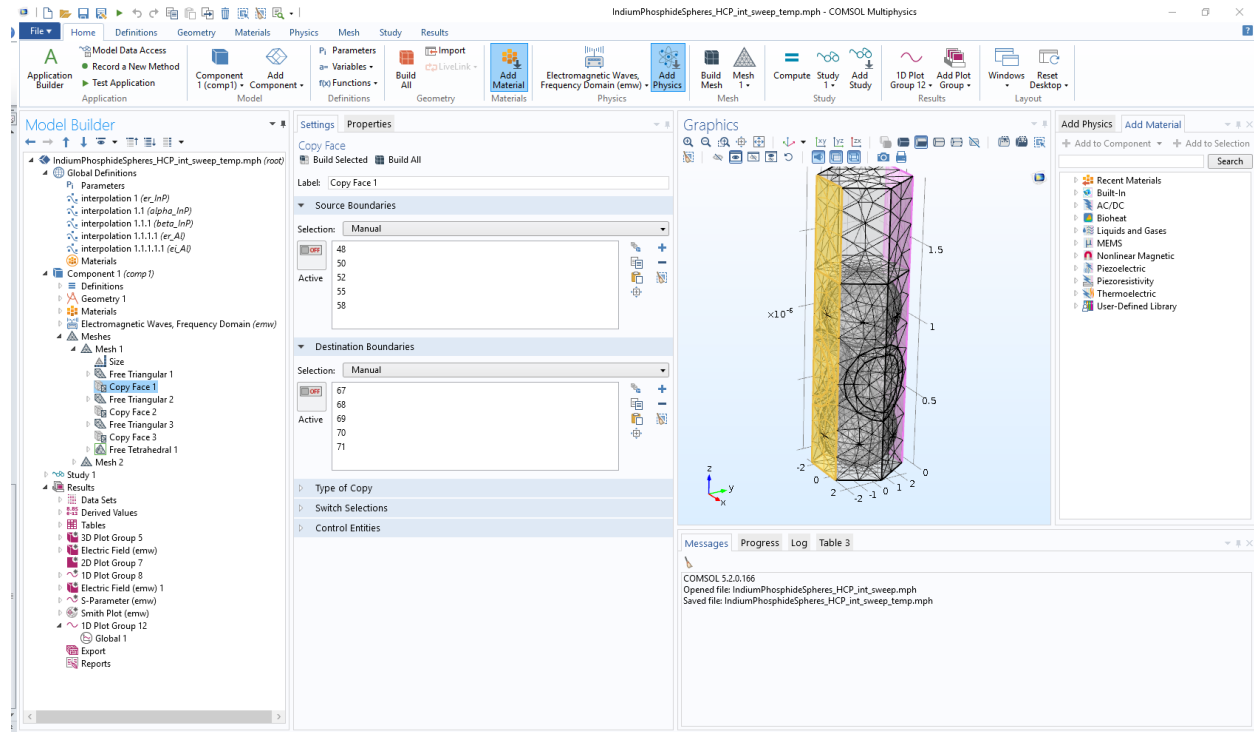


Figure 6. Copying the mesh from one side of the unit cell to the opposite face.

Next is the Study setup. Right-click Study, go to Study Steps, Select Frequency Domain twice. To perform a frequency sweep, within the Frequency Domain Study Settings, in the Frequencies field enter the range as range (230 [THz],2 [THz],340 [THz]) . Or enter a single frequency as 100 [THz]. Parametric sweeps, for example of intensity, can be set up by right-clicking Study and selecting Parametric Sweep. Then in the Study Settings of Parametric Sweep, simply select the parameter name and enter the values separated by commas. To perform the simulation, right-click Study and select Compute.

Finally, the last step is to set up plots. For example, to generate a 1D plot, right-click Results and select 1D Plot Group. In the y-Axis Data field, enter the quantity desired such as $\text{abs}(\text{emw.S11})^2$ for reflection coefficient. To plot frequency on the x axis, enter freq in the Expression field under x-Axis Data, or to plot the sweep parameter simply select parameter value under x-Axis Data.

Appendix C

**Manuscript entitled “Nonlinear absorption in dielectric metamaterials,”
prepared for possible publication in Applied Physics Letters**

Nonlinear absorption in dielectric metamaterials

B. Slovick, L. Zipp, and S. Krishnamurthy

SRI International, Applied Optics Laboratory, 333 Ravenswood Avenue, Menlo Park, California 94025

Abstract: We solve the nonlinear Maxwell equations in an InP-based dielectric metamaterial, considering both two-photon absorption and photo-induced free-carrier absorption. We obtain the intensity-dependent reflection, absorption, and effective permittivity and permeability of the metamaterial. Our results show that nonlinear absorption dampens both the electric and magnetic resonance, although the magnetic resonance is more affected because it occurs at longer wavelengths where the free-carrier absorption cross section is larger. Owing to field concentration in the metamaterial at resonance, the threshold intensity for nonlinear absorption is smaller by a factor of about 30 compared to a homogeneous layer of the same thickness. Our results have implications on the use of dielectric metamaterials for nonlinear applications such as frequency conversion and optical limiting.

Materials with strong nonlinear response are desired for applications involving optical limiting [1-3], ultrafast modulation [4-6], frequency conversion [7,8], and optical isolation [9,10]. Traditional bulk materials have a weak interaction between electron and sub-bandgap photons, as indicated by measured nonlinear absorption coefficients [11-14], and thus require high intensities or long interaction lengths to achieve an efficient nonlinear response.

One way to enhance the nonlinear response is to incorporate metamaterial elements or plasmonic structures to concentrate the electric fields within a nonlinear material [15,16]. Metamaterials containing plasmonic nanostructures have been integrated with nonlinear materials to enhance second-harmonic generation [17-23] and achieve analog electromagnetically induced transparency (EIT) [24,25]. The drawback of plasmonic approaches is that the fields are highly localized at the metal dielectric interface, leading to small interaction volumes [26,27]. Also, the finite conductivity of metals at optical frequencies leads to undesirable losses. An alternative approach is to induce nonlinearity in dielectric metamaterials using Mie or Fano resonances. Dielectric nanostructures have been used to enhance third-harmonic generation [26-31] and to achieve ultrafast optical modulation [32-34].

To date, the research on nonlinear phenomena in dielectric metamaterials has focused primarily on the experimental aspects [26-31], with relatively few examples of theoretical studies. A few examples employ the recently-developed linear generalized source method for nonlinear materials [35-37], which calculates the diffraction of one- and two-dimensional gratings accounting for nonlinear polarization sources. Although these models provide important insights, they do not support three-dimensional structures and do not represent full solutions of the nonlinear Maxwell equations. Also, existing models do not account for the nontrivial frequency dependence of the nonlinear parameters, such as the two photon absorption (TPA) coefficient and the free-carrier absorption (FCA) cross section [14].

In this work, we develop a full-wave model to solve the nonlinear Maxwell equations in a structured, three-dimensional metamaterial accounting for both TPA and photo-induced FCA. The nonlinear absorption coefficients are obtained from full-band structure calculations [14]. We apply the model to study the optical properties and effective parameters of a representative InP-based dielectric

metamaterial operating in the near infrared spectral band. As expected, we find that nonlinear absorption at high intensities leads to dampening of the electric and magnetic Mie resonances. For continuous wave illumination, the onset nonlinear absorption occurs at intensities around 1 MW/cm^2 , while the Mie resonances are almost completely diminished for intensities approaching 5 MW/cm^2 . In addition, we find several unexpected results. First, the nonlinear absorption at the magnetic resonance is larger than at electric resonance, which can be explained by the wavelength-dependent FCA. Second, assuming FCA is independent of wavelength, the absorption at the two resonances is found to be nearly equal, despite the electric field being heavily localized at the electric resonance and more uniformly distributed at the magnetic resonance. Third, owing to the enhancement of the electric field at resonance, we find that the intensity threshold of nonlinear absorption in the metamaterial is nearly 30 times lower than for a homogeneous material of similar thickness.

To illustrate more clearly the effects of nonlinearity on Mie resonances, we consider a large index-contrast metamaterial consisting of 360 nm InP spheres with large refractive index (3.3) in air medium, arranged in a square lattice with a periodicity of 800 nm, as shown in Fig. 1a. InP is chosen for its transparency in the near-infrared band of interest ($0.9\text{-}1.3 \mu\text{m}$). The conclusions drawn in this article are valid even if the air medium is replaced by a polymer and the metamaterial layer is placed on a low index substrate such as silica. The size and periodicity of the InP spheres are optimized to position the electric and magnetic Mie resonances, identified as narrowband peaks in the reflection spectrum, in the band of interest as shown in Fig. 1(b).

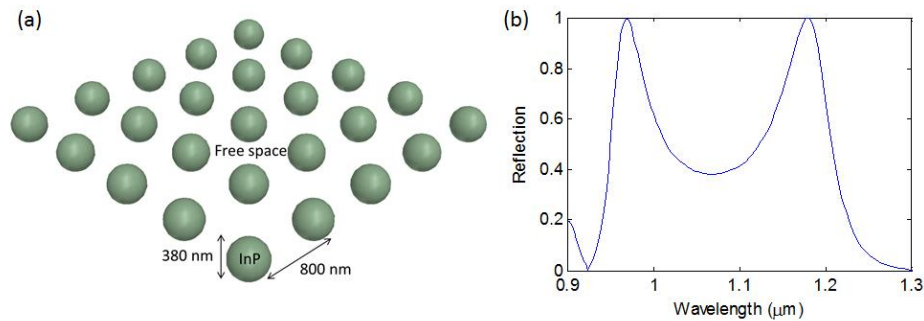


Figure 1. (a) Dielectric metamaterial consisting of InP spheres in free space. (b) The calculated reflection spectrum for low intensities, showing two peaks corresponding to the electric and magnetic resonances.

The origin of nonlinear absorption in InP can be understood from the band structure, shown in Fig. 2. The valence bands (VBs) consist of heavy-hole (HH), light-hole (LH), and spin-orbit (SO) bands. The conduction band (CB) is separated from the HH band by the band gap. In the absence of light, states in the VB are filled with electrons and the CB states are empty. Electrons in the VB can absorb photons with energy larger than the band gap and enter the CB. Since the band gap of InP (1.45 eV) is larger than the photon energies in the band of interest ($0.9\text{-}1.4 \text{ eV}$), at low intensities photons transmit through InP without absorption. However, when the incident intensity is high, the probability for valence electrons to absorb two photons (shown as two stacked vertical arrows) is high, resulting in reduced transmission. In addition, this TPA is followed by FCA in which the holes left behind

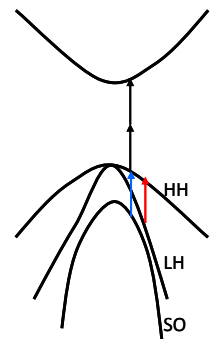


Figure 2. Band structure of InP.

in the HH band can be filled by one-photon absorption by electrons in the LH and SO bands, shown by the colored arrows in Fig. 2. Because the strength of both TPA and FCA depend on intensity, they are referred to as nonlinear absorption processes. Figure 3 shows the previously calculated values of TPA coefficient β and the FCA cross section σ for InP [14]. The value of β is relatively constant with wavelength, which is typical for wide-bandgap materials, while σ increases by an order of magnitude over the band. The FCA increases with increasing wavelength because the corresponding photon energy decreases, and the energy-momentum conservation condition for FCA (colored lines in Figure 2) is satisfied only near the center of the Brillouin zone, where a larger number of holes are present.

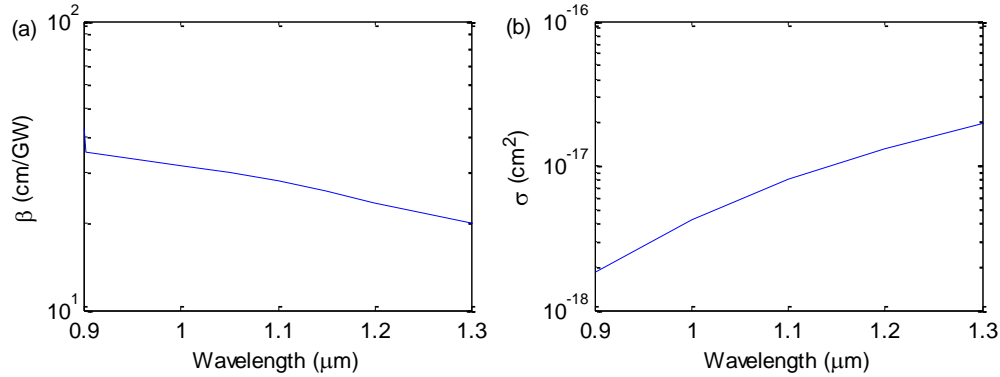


Figure 3. Wavelength dependence of the two-photon absorption coefficient (a) and free-carrier absorption cross section (b) for InP.

We will now incorporate these nonlinear coefficients into Maxwell's equations. The nonlinear Maxwell equation for the electric field $E(\mathbf{r}, t)$ is [38,39]

$$\nabla^2 E(\mathbf{r}, t) - \frac{n^2}{c^2} \frac{\partial^2 E(\mathbf{r}, t)}{\partial t^2} - \frac{1}{\epsilon_0 c^2} \frac{\partial^2 P_{NL}(\mathbf{r}, t)}{\partial t^2} - \frac{n\sigma N}{c} \frac{\partial E(\mathbf{r}, t)}{\partial t} = 0, \quad (1)$$

where n is the refractive index of the medium, c is the speed of light, N and σ are the free-carrier concentration and absorption cross section, and ϵ_0 is the free-space permittivity. The nonlinear polarization P_{NL} is related to the third-order nonlinear susceptibility $\chi^{(3)}$ by

$$P_{NL}(\mathbf{r}, t) = \frac{3}{4} \epsilon_0 \chi^{(3)} |E(\mathbf{r}, t)|^2 E(\mathbf{r}, t). \quad (2)$$

Substituting Eq. (2) into Eq. (1) and assuming monochromatic solutions $E(\mathbf{r}, t) = E(\mathbf{r}) \exp(-i\omega t)$, we obtain

$$\left(\nabla^2 + n^2 \frac{\omega^2}{c^2} + \frac{3}{4} \frac{\omega^2}{c^2} \chi^{(3)} |E(\mathbf{r})|^2 + i\omega \frac{n\sigma N}{c} \right) E(\mathbf{r}) = 0. \quad (3)$$

Relating the imaginary part of $\chi^{(3)}$ to the two-photon absorption coefficient β as [38,39]

$$\text{Im}(\chi^{(3)}) = \frac{2n^2 c^2 \epsilon_0}{3\omega} \beta,$$

and neglecting the real part of $\chi^{(3)}$, Eq. (3) can be rewritten as

$$\left(\nabla^2 + n^2 \frac{\omega^2}{c^2} + i \frac{1}{2} \beta \omega n^2 \epsilon_0 |E(\mathbf{r})|^2 + i\omega \frac{n\sigma N}{c} \right) E(\mathbf{r}) = 0. \quad (4)$$

The free carrier concentration is given by the continuity equation for free electrons [14,38,39]

$$\frac{dN}{dt} = \frac{\beta I^2}{2\hbar\omega} - \frac{N}{\tau}, \quad (5)$$

where $\hbar\omega$ is the photon energy and τ is the photo-carrier relaxation time, which we assume is a constant equal to 1 μ s. The first term in Eq. (5) describes free-carrier generation via two-photon absorption, and the second term describes free carrier recombination. For continuous-wave illumination, the free-carrier concentration will reach steady state conditions ($dN/dt=0$) and thus

$$N(I) = \frac{\beta\tau}{2\hbar\omega} I^2. \quad (6)$$

Substituting Eq. (6) into Eq. (4) and using the relation between the intensity and the electric field $I = nc\varepsilon_0 |E(\mathbf{r})|^2 / 2$, we obtain the following form of the nonlinear Maxwell equation:

$$\left(\nabla^2 + n^2 \frac{\omega^2}{c^2} + i \frac{1}{2} \beta \omega n^2 \varepsilon_0 |E(\mathbf{r})|^2 + i \frac{\sigma \beta \tau n^3 c \varepsilon_0^2}{8\hbar} |E(\mathbf{r})|^4 \right) E(\mathbf{r}) = 0. \quad (7)$$

We use the full-wave finite-element frequency domain solver in COMSOL to solve Eq. 7. Before applying Eq. (7) to the metamaterial in Fig.1, we apply it to a homogeneous nonlinear medium and compare the results with the solution to the well-known rate equation [38,39]

$$\frac{dI}{dx} = -\beta I^2 - \frac{\sigma \beta \tau}{2\hbar\omega} I^3. \quad (8)$$

The transmitted intensity, as a function of thickness for InP at a wavelength of 1 μ m for various intensities, calculated by solving Eq. (7) and (8), respectively, are shown by dots and solid lines in Fig. 4. The two calculations are in excellent agreement, thus validating our full-wave nonlinear model. In this validation the index of InP is set equal to 1 to avoid interference effects due to interface reflections.

We now apply our validated nonlinear full-wave model (Eq. 7) to understand the role of nonlinear absorption in the dielectric metamaterial shown in Fig. 1(a). First, we studied the reflection and absorption for different incident intensities, shown in Fig. 5. For all intensities, the reflection spectrum contains narrowband peaks near 1.2 and 0.95 μ m, corresponding to the magnetic and electric dipole Mie resonances, respectively. For a low intensity of 1 W/cm², the nonlinear processes are negligible, resulting in low absorption and nearly 100% reflection at the two resonances. As the intensity increases, the absorption at the resonances increases and the reflection decreases.

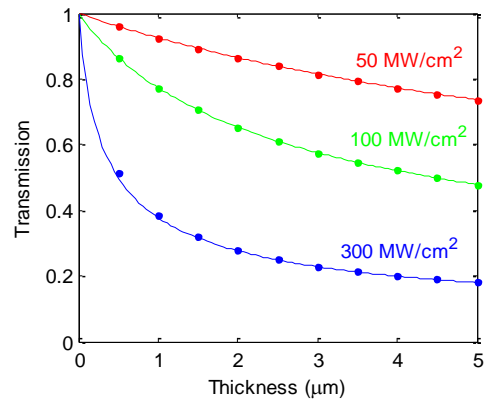


Figure 4. Transmission of bulk InP as a function of thickness for different incident intensities, calculated using nonlinear full-wave COMSOL (dots) and by numerically integrating Eq. (8) (solid lines).

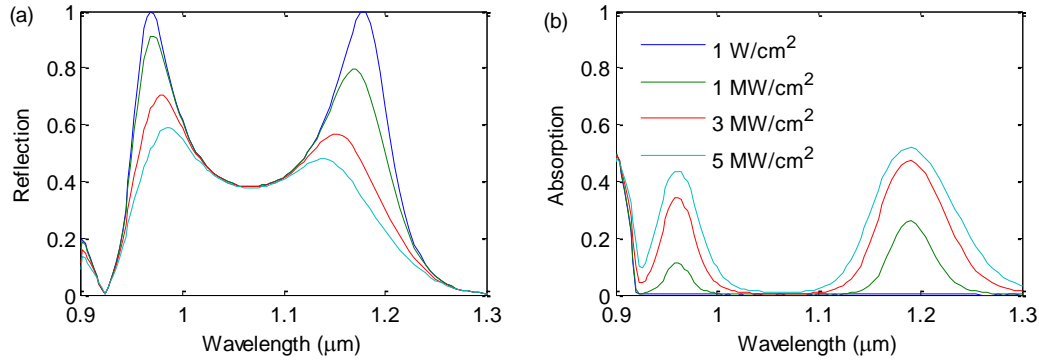


Figure 5. Wavelength dependence of the reflection (a) and absorption (b) for a $0.8 \mu\text{m}$ square array of 360-nm diameter InP spheres for different incident intensities.

We note that for a given intensity, the absorption is larger at the magnetic resonance ($1.2 \mu\text{m}$) than at the electric resonance ($0.95 \mu\text{m}$). This can be understood from the electric field distributions at the resonances, shown in Fig. 6(a) and (b) normalized to the incident electric field for an intensity of $1 \text{ MW}/\text{cm}^2$. At the magnetic dipole resonance, the electric field is ring shaped and relatively uniform, while the electric field at the electric dipole resonance is highly concentrated at the center of the sphere. Note the field concentration outside the sphere arises from the boundary condition on the normal component electric field, which is discontinuous by the ratio of the dielectric constants of the sphere and free space. Thus, based on the field distributions, one might expect the absorption at the electric resonance to be larger due to the larger field concentration. However, we find more absorption at the magnetic resonance. We attribute this to the FCA cross section being about 5 times larger at the magnetic resonance than at the electric resonance (Fig. 3b). To validate this claim, we recalculated the spectral absorption for $1 \text{ MW}/\text{cm}^2$ intensity assuming a constant FCA cross section. The results, shown in Fig. 6(c), show that the absorption is approximately equal at the two resonances, confirming that the wavelength-dependent FCA cross section is responsible for the larger absorption at the magnetic resonance. The fact that the absorption is equal at the two resonances for constant FCA is also counterintuitive, since more absorption is expected at the electric resonance because of the field concentration.

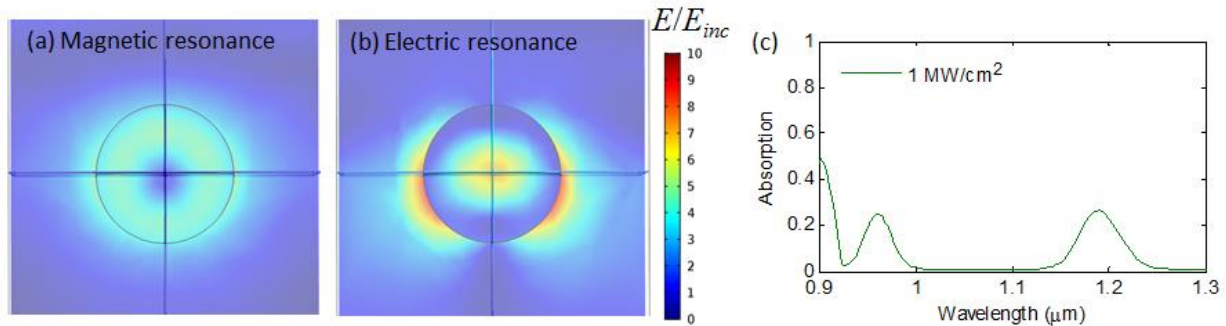


Figure 6. Electric field distributions, normalized to the incident field, at the magnetic resonance (a) and electric resonance (b) for an incident intensity of $1 \text{ MW}/\text{cm}^2$. (c) Absorption of the metamaterial for an intensity of $1 \text{ MW}/\text{cm}^2$, assuming a constant free carrier absorption cross section.

Since the electric field is enhanced at both resonances, we expect more absorption per unit length in the metamaterial than in a homogeneous material. To illustrate this, we calculated the reflection and absorption of a 360 nm-thick slab of InP, equal in thickness to the InP sphere metamaterial in Fig. 1(a). We see from Fig. 7 that 100 MW/cm² of intensity is needed to obtain 40% absorption near 1.2 μ m in the homogenous layer, whereas the metamaterial obtains a similar level of absorption for 3 MW/cm². Thus, the homogenous layer requires much higher intensities to achieve absorption values comparable to the metamaterial. This factor of 30 higher intensity is consistent with the five-fold field enhancement at the magnetic resonance shown in Fig. 6(a).

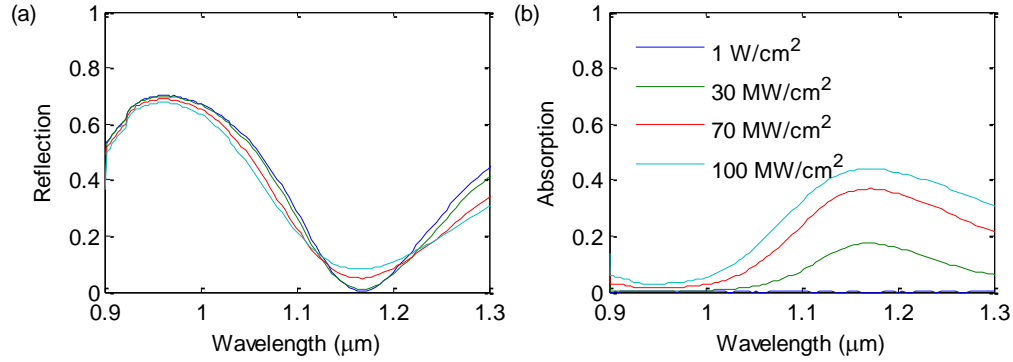


Figure 7. Wavelength dependence of the reflection (a) and absorption (b) for a 360 nm thick film of InP for different incident intensities.

It is also important to understand the impact of nonlinear absorption on the effective permittivity (ϵ) and permeability (μ) of the metamaterial, as they are often used to obtain unique properties such as negative refraction and perfect reflection. The calculated real (ϵ) and real (μ), shown in Fig. 8, were obtained using S-parameter inversion, assuming a layer thickness of 1.24 μ m. At low intensities, shown as the blue line in Fig. 8(a), we see a strong resonance in μ near 1.2 μ m, which arises from the magnetic resonance. The weaker resonance near 0.95 μ m is the anti-resonance associated with the strong electric resonance at that wavelength, which is clearly seen in Fig. 8b for the permittivity. We also find a strong anti-resonance in ϵ at 1.1 μ m, which arises from the magnetic resonance at 1.2 μ m. These anti-resonances are an artifact of S-parameter retrieval that arises from approximating a Bloch wave by a plane wave [40]. In the resonance regions, either ϵ or μ is negative, resulting in single-negative regions, which results in high reflectivity as shown in Fig. 5(a). As the intensity increases to 1 MW/cm² and 3 MW/cm², we find that the magnetic resonance (near 1.2 μ m in Fig. 8a) begins to dampen while the electric resonance (near 1 μ m in Fig. 8b) is largely unchanged. Only when the intensity exceeds 3 MW/cm² does the electric resonance begin to dampen. For 5 MW/cm², both resonances are completely dampened. The dampening of the resonances with increasing intensity is also consistent with the decreasing reflection in Fig. 5(a). As the resonance in the real part of ϵ and μ broadens, the corresponding imaginary part of ϵ and μ (not shown) also broadens, as per the Kramer-Kronig relationship, which results in broader band absorption with intensity as shown in Fig. 5(b).

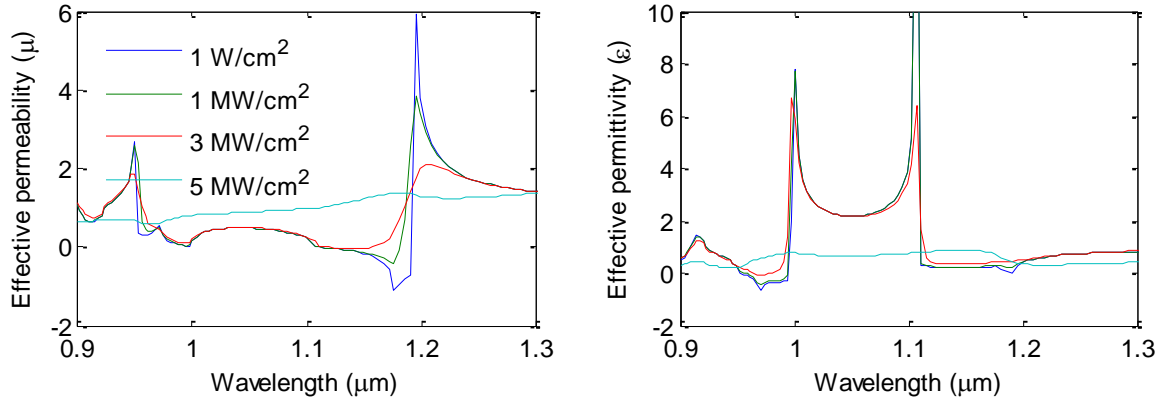


Figure 8. Wavelength dependence of the effective permeability and permittivity of the InP metamaterial for different incident intensities.

In summary, we developed a full-wave model to study the effects of two-photon absorption and photo-induced free-carrier absorption on the effective parameters and optical properties of a structured dielectric metamaterial. As expected, we find that nonlinear absorption leads to dampening of the electric and magnetic Mie resonances at high intensities, with an onset around 1 MW/cm^2 , assuming continuous wave illumination. The resonances are almost completely dampened for intensities around 5 MW/cm^2 . Surprisingly, we find that the nonlinear absorption at the magnetic resonance is larger than at the electric resonance, despite the electric field being more concentrated at the electric resonance. We find this is because the free-carrier absorption cross section is considerably larger at the longer wavelengths near the magnetic resonance. We also find that the metamaterial provides absorption comparable to a homogeneous layer of the same thickness at approximately 30 times less intensity. The lower threshold intensity and smaller footprint for nonlinear absorption can be exploited in applications involving optical limiting, frequency conversion, the Kerr effect, and four-wave mixing.

References

1. Van Stryland, E.W., Vanherzeele, H., Woodall, M.A., Soileau, M.J., Smirl, A.L., Guha, S. and Boggess, T.F., 1985. Two photon absorption, nonlinear refraction, and optical limiting in semiconductors. *Optical Engineering*, 24(4), pp.244613-244613.
2. Boggess, T., Smirl, A., Moss, S., Boyd, I. and Van Stryland, E., 1985. Optical limiting in GaAs. *IEEE journal of quantum electronics*, 21(5), pp.488-494.
3. Van Stryland, E.W., Wu, Y.Y., Hagan, D.J., Soileau, M.J. and Mansour, K., 1988. Optical limiting with semiconductors. *JOSA B*, 5(9), pp.1980-1988.
4. Scalora, M., Dowling, J.P., Bowden, C.M. and Bloemer, M.J., 1994. Optical limiting and switching of ultrashort pulses in nonlinear photonic band gap materials. *Physical review letters*, 73(10), p.1368.
5. Tran, P., 1997. Optical limiting and switching of short pulses by use of a nonlinear photonic bandgap structure with a defect. *JOSA B*, 14(10), pp.2589-2595.
6. Haché, A. and Bourgeois, M., 2000. Ultrafast all-optical switching in a silicon-based photonic crystal. *Applied Physics Letters*, 77(25), pp.4089-4091.
7. Rashkeev, S.N. and Lambrecht, W.R., 2001. Second-harmonic generation of I-III-VI 2 chalcopyrite semiconductors: Effects of chemical substitutions. *Physical Review B*, 63(16), p.165212.

8. Lekse, J.W., Moreau, M.A., McNerny, K.L., Yeon, J., Halasyamani, P.S. and Aitken, J.A., 2009. Second-harmonic generation and crystal structure of the diamond-like semiconductors Li₂CdGeS₄ and Li₂CdSnS₄. *Inorganic chemistry*, 48(16), pp.7516-7518.
9. Gallo, K. and Assanto, G., 1999. All-optical diode based on second-harmonic generation in an asymmetric waveguide. *JOSA B*, 16(2), pp.267-269.
10. Yu, Z. and Fan, S., 2009. Complete optical isolation created by indirect interband photonic transitions. *Nature photonics*, 3(2), pp.91-94.
11. Chang, D.E., Vuletić, V. and Lukin, M.D., 2014. Quantum nonlinear optics [mdash] photon by photon. *Nature Photonics*, 8(9), pp.685-694.
12. Bechtel, J.H. and Smith, W.L., 1976. Two-photon absorption in semiconductors with picosecond laser pulses. *Physical Review B*, 13(8), p.3515.
13. Boggess, T., Bohnert, K., Mansour, K., Moss, S., Boyd, I. and Smirl, A., 1986. Simultaneous measurement of the two-photon coefficient and free-carrier cross section above the bandgap of crystalline silicon. *IEEE journal of quantum electronics*, 22(2), pp.360-368.
14. Krishnamurthy, S., Yu, Z.G., Gonzalez, L.P. and Guha, S., 2011. Temperature-and wavelength-dependent two-photon and free-carrier absorption in GaAs, InP, GaInAs, and InAsP. *Journal of Applied Physics*, 109(3), p.033102.
15. M. Kauranen and A. V. Zayats, *Nat. Photon.* 6, 737 (2012).
16. Schuller, J.A., Barnard, E.S., Cai, W., Jun, Y.C., White, J.S. and Brongersma, M.L., 2010. Plasmonics for extreme light concentration and manipulation. *Nature materials*, 9(3), pp.193-204.
17. Czaplicki, R., Husu, H., Siikanen, R., Mäkitalo, J., Kauranen, M., Laukkanen, J., Lehtolahti, J. and Kuittinen, M., 2013. Enhancement of second-harmonic generation from metal nanoparticles by passive elements. *Physical review letters*, 110(9), p.093902.
18. Aouani, H., Navarro-Cia, M., Rahmani, M., Sidiropoulos, T.P., Hong, M., Oulton, R.F. and Maier, S.A., 2012. Multiresonant broadband optical antennas as efficient tunable nanosources of second harmonic light. *Nano letters*, 12(9), pp.4997-5002.
19. Thyagarajan, K., Rivier, S., Lovera, A. and Martin, O.J., 2012. Enhanced second-harmonic generation from double resonant plasmonic antennae. *Optics express*, 20(12), pp.12860-12865.
20. Thyagarajan, K., Butet, J. and Martin, O.J., 2013. Augmenting second harmonic generation using Fano resonances in plasmonic systems. *Nano letters*, 13(4), pp.1847-1851.
21. Zhang, Y., Grady, N.K., Ayala-Orozco, C. and Halas, N.J., 2011. Three-dimensional nanostructures as highly efficient generators of second harmonic light. *Nano letters*, 11(12), pp.5519-5523.
22. Harutyunyan, H., Volpe, G., Quidant, R. and Novotny, L., 2012. Enhancing the nonlinear optical response using multifrequency gold-nanowire antennas. *Physical review letters*, 108(21), p.217403.
23. Navarro-Cia, M. and Maier, S.A., 2012. Broad-band near-infrared plasmonic nanoantennas for higher harmonic generation. *ACS nano*, 6(4), pp.3537-3544.
24. Gu, J., Singh, R., Liu, X., Zhang, X., Ma, Y., Zhang, S., Maier, S.A., Tian, Z., Azad, A.K., Chen, H.T. and Taylor, A.J., 2012. Active control of electromagnetically induced transparency analogue in terahertz metamaterials. *Nature communications*, 3, p.1151.
25. Kurter, C., Tassin, P., Zhang, L., Koschny, T., Zhuravel, A.P., Ustinov, A.V., Anlage, S.M. and Soukoulis, C.M., 2011. Classical analogue of electromagnetically induced transparency with a metal-superconductor hybrid metamaterial. *Physical review letters*, 107(4), p.043901.
26. Shcherbakov, M.R., Neshev, D.N., Hopkins, B., Shorokhov, A.S., Staude, I., Melik-Gaykazyan, E.V., Decker, M., Ezhov, A.A., Miroshnichenko, A.E., Brener, I. and Fedyanin, A.A., 2014. Enhanced third-harmonic generation in silicon nanoparticles driven by magnetic response. *Nano letters*, 14(11), pp.6488-6492.

27. Yang, Y., Wang, W., Boulesbaa, A., Kravchenko, I.I., Briggs, D.P., Puretzky, A., Geohegan, D. and Valentine, J., 2015. Nonlinear Fano-resonant dielectric metasurfaces. *Nano letters*, 15(11), pp.7388-7393.
28. Shcherbakov, M.R., Shorokhov, A.S., Neshev, D.N., Hopkins, B., Staude, I., Melik-Gaykazyan, E.V., Ezhov, A.A., Miroshnichenko, A.E., Brener, I., Fedyanin, A.A. and Kivshar, Y.S., 2015. Nonlinear interference and tailorable third-harmonic generation from dielectric oligomers. *ACS Photonics*, 2(5), pp.578-582.
29. Smirnova, D.A., Khanikaev, A.B., Smirnov, L.A. and Kivshar, Y.S., 2016. Multipolar third-harmonic generation driven by optically induced magnetic resonances. *ACS Photonics*, 3(8), pp.1468-1476.
30. Grinblat, G., Li, Y., Nielsen, M.P., Oulton, R.F. and Maier, S.A., 2016. Enhanced third harmonic generation in single germanium nanodisks excited at the anapole mode. *Nano letters*, 16(7), pp.4635-4640.
31. Shorokhov, A.S., Melik-Gaykazyan, E.V., Smirnova, D.A., Hopkins, B., Chong, K.E., Choi, D.Y., Shcherbakov, M.R., Miroshnichenko, A.E., Neshev, D.N., Fedyanin, A.A. and Kivshar, Y.S., 2016. Multifold enhancement of third-harmonic generation in dielectric nanoparticles driven by magnetic Fano resonances. *Nano Letters*, 16(8), pp.4857-4861.
32. Shcherbakov, M.R., Vabishchevich, P.P., Shorokhov, A.S., Chong, K.E., Choi, D.Y., Staude, I., Miroshnichenko, A.E., Neshev, D.N., Fedyanin, A.A. and Kivshar, Y.S., 2015. Ultrafast all-optical switching with magnetic resonances in nonlinear dielectric nanostructures. *Nano letters*, 15(10), pp.6985-6990.
33. Makarov, S., Kudryashov, S., Mukhin, I., Mozharov, A., Milichko, V., Krasnok, A. and Belov, P., 2015. Tuning of magnetic optical response in a dielectric nanoparticle by ultrafast photoexcitation of dense electron-hole plasma. *Nano letters*, 15(9), pp.6187-6192.
34. Baranov, D.G., Makarov, S.V., Milichko, V.A., Kudryashov, S.I., Krasnok, A.E. and Belov, P.A., 2016. Nonlinear transient dynamics of photoexcited resonant silicon nanostructures. *ACS Photonics*, 3(9), pp.1546-1551.
35. Weismann, M., Gallagher, D.F. and Panoiu, N.C., 2015. Nonlinear generalized source method for modeling second-harmonic generation in diffraction gratings. *JOSA B*, 32(4), pp.523-533.
36. Weismann, M. and Panoiu, N.C., 2016. Theoretical and computational analysis of second-and third-harmonic generation in periodically patterned graphene and transition-metal dichalcogenide monolayers. *Physical Review B*, 94(3), p.035435.
37. Kruk, S., Weismann, M., Bykov, A.Y., Mamonov, E.A., Kolmychek, I.A., Murzina, T., Panoiu, N.C., Neshev, D.N. and Kivshar, Y.S., 2015. Enhanced magnetic second-harmonic generation from resonant metasurfaces. *ACS Photonics*, 2(8), pp.1007-1012.
38. Shen, Y.R., 1984. *The principles of nonlinear optics*. New York, Wiley-Interscience, 1984, 575 p., 1.
39. Stegeman, G.I. and Stegeman, R.A., 2012. *Nonlinear Optics: Phenomena, Materials and Devices (Vol. 78)*. John Wiley & Sons.
40. Koschny, T., Markoš, P., Smith, D.R. and Soukoulis, C.M., 2003. Resonant and antiresonant frequency dependence of the effective parameters of metamaterials. *Physical Review E*, 68(6), p.065602.